Title: Variation of magnetization dynamics of LSMO/Pt bilayer with temperature.

Presenter: Biswajit Sahoo
Lab Group: Dr. Eric Fullerton

Energy efficient oscillators are essential for development of low-power neuromorphic computing systems. Commonly used oscillator material systems are all metallic bilayers of Ferromagnet(FM)/ Heavy metal(HM) (FM=CoFeB, Py, NM=Pt, Ta, W) with a relatively high intrinsic Gilbert damping of the order of 10^{-2}. Large spin-charge conversion, low damping, and small resonance linewidth are essential constituents for development of energy efficient oscillators. In this regard a bilayer thin film of half-metallic perovskite ferromagnet, namely $La_{0.67}Sr_{0.33}MnO_3$ (LSMO) and Pt may be a potential material system to develop such oscillators. LSMO has a very low damping and nearly 100% spin polarization, whereas Pt is metallic with a large charge to spin conversion efficiency. Further the magnetization of LSMO increases with low temperatures, which can give large spin-torque signals. All these properties prompt us to study the variation of magnetization dynamics of LSMO(13nm) /Pt(5nm) system with temperature. We employ temperature dependent co-planar waveguide ferromagnetic resonance and temperature dependent spin-pumping ferromagnetic resonance to extract the various magnetic parameters and the charge to spin conversion efficiency in this bilayer system. We find that the system exhibits lowest damping (0.002) and small linewidth (12Oe) and a large spin Hall angle (≈ 4%) at 170K, making it the best working temperature for spin Hall nano-oscillators made out of this bilayer.

Spin-Orbit Studies of Ferrimagnetic and Antiferromagnetic Weyl Semimetals

Eric Fullerton; University of California-San Diego, United States

Topology has emerged in many areas of magnetism that included both chiral spin structures and emergent electronic structures such as Weyl semimetals. The further lowering of the symmetry of the crystal via strain or magnetic order can provide additional functionality. I will discuss recent studies of thin films of candidate Weyl semimetals and their potential use as sources of spin currents in spin-orbit torque devices. Materials studies include ferrimagnetically ordered $CrPt_3$, antiferromagnetically ordered $FePt_3$ and FeRh. For each we have grown epitaxial chemically ordered films and studied the spin structure, magneto-transport properties, and spin-to-charge conversion that is a source for spin-orbit torques. I will highlight the potential uses for complex materials that generate large, tunable spin-orbit torques. They may be used in conventional computing to non-volatile memory schemes, or for neuromorphic computing approaches exploiting spin dynamics in more complex magnetic systems.

This work is supported by US Department of Energy under Grant No. DESC0019273

Control Crystallinity and Polarity of GaN on Oxide-free Si (111) Using ALD Process Parameters

[1]S. Yun, [1]P. Lee, [2]J. Spiegelman, [3]W. Aigner, [3]T. Metzger and [1]A. Kummel*
[1]*University of California, San Diego*
[2]*RASIRC Inc., San Diego, CA, United States*
[3]*Qualcomm Germany RFFE GmbH, Munich, Germany*

The control of crystallinity and polarity of III-V semiconductors have key roles in the improvement of the performance in electronic applications. Wurtzite gallium nitride (GaN) has been extensively studied for optoelectronics, power electronics operated at high voltage/temperature, and buffer layers for other III-V semiconductors [1]. The atomic layer annealing (ALA) was reported to improve the crystallinity of the III-V compounds (aluminum nitride) at low temperatures as compared to the conventional thermal ALD by Ueda et al. and Shih et al. [2,3]. 100 nm of SiO_2 and sapphire substrates were reported to deposit crystallized GaN ALA films using krypton process gas by UCSD. Li et al. reported that GaN polarity on sapphire substrates using the selective wet etching of KOH solution with various techniques other than atomic layer deposition (ALD) [4]. However, the crystallinity and polarity of GaN ALD films on inert, oxide-free Si (111) have not been widely studied yet because of the lattice mismatch (~16%) and coefficient of thermal expansion mismatch (~54 %) [5].

Thermal ALD, ALA, and GaN stacks (GaN thermal ALD/ALA and GaN ALA/thermal ALD/ALA) were investigated to control the crystallinity and polarity of GaN on oxide-free Si (111) substrates. The native Si oxide was removed by dipping in 2 wt.% HF solution. The self-limiting ALD growth was achieved with N_2H_4 (Rasirc) and TDMAGa (EMD) (not shown). Table 1 summarized the optimized plasma pulse length during ALA process, suggesting smooth and crystallized high-quality GaN ALD layers were deposited during 15 s of the GaN ALA process.

Figure 1a shows that the intensity of GaN (002) XRD pattern in GaN thermal ALD on Si was drastically improved in the GaN stacks (GaN thermal ALD/ALA/Si) with GaN ALA buffer layer. The similar crystallinity of GaN ALA and GaN stack (GaN ALA/thermal ALD/ALA/Si) suggested the insignificant impact of the inserted GaN thermal ALD layers on the crystallinity of top GaN ALD layers. Figure 1b-c show the top-view SEM image of selectively wet-etched GaN films after 30 min dipping in KOH aqueous solution. The significantly etched surface on the GaN ALA layers (Figure 1b) indicated N-polar GaN surface since the KOH could be a catalyst in the reaction ($2\ GaN + 3\ H_2O \rightarrow Ga_2O_3 + 2\ NH_3$) with N-polar GaN [4]. Figure 1c shows a nearly unchanged GaN surface in GaN thermal ALD layers on GaN ALA buffered Si (111), suggesting the Ga-polar GaN surface because of large repulsion between Ga-polar GaN and OH^- ion.

Figure 2a shows a homogeneously deposited columnar growth of GaN films with 10-20 nm grains in the HR-TEM of GaN ALA on Si (111). Figure 2b displays the polycrystalline of GaN with poor crystallinity near the interface due to lattice mismatch. The crystallinity of GaN ALA layers was improved as growing GaN layers. The high-angle annular dark field (HAADF) STEM image (Figure 2c) demonstrates highly ordered 3 nm x 5 nm GaN ALD layers with bright and dark regions. The circles of bright regions and the center of dark regions represent Ga atoms and tunnel points (empty element), respectively. The GaN polarity could be determined by drawing triangles connecting adjacent tunnel points without the interruption of Ga. Upward triangles suggested the formation of N-polar GaN layers during the GaN ALA process on Si in good agreement with the wet-etched SEM image (Figure 1b).

1. T. Flack et al., *Journal of Electronic Materials*, 45, **2016,** 2673-2682
2. S. Ueda et al., " *Journal of Materials Chemistry C*, 10, **2022,** 5707-5715
3. H. Shih et al., *Scientific Reports*, 7, **2017,** 39717
4. D. Li et al., *Journal of Applied Physics*, 90, **2001,** 4219-4223 doi:10.1063/1.1402966
5. S. Pal and C. Jacob, *Bulletin of Materials Science*, 27, **2004,** 501-504

Table 1. Summary of GPCs, densities, FWHM, peak positions of GaN (002) XRD patterns, thickness, and RMS for the GaN ALA films with 0-30 s plasma length.

Sample	0 s (Thermal)	10 s	15 s	20 s	30 s
GPC (Å/cyc)	1.4	0.9	1.2	1.2	1.3
Density (g/cm^3)	6.1	6.1	6.0	6.1	6.1
FWHM (°)	1.21	0.74	0.59	0.68	1.20
Peak (°)	34.5	34.5	34.5	34.5	34.4
Thickness (nm)	42	28	36	36	38
RMS (nm)	0.6	0.7	1.0	1.0	0.7

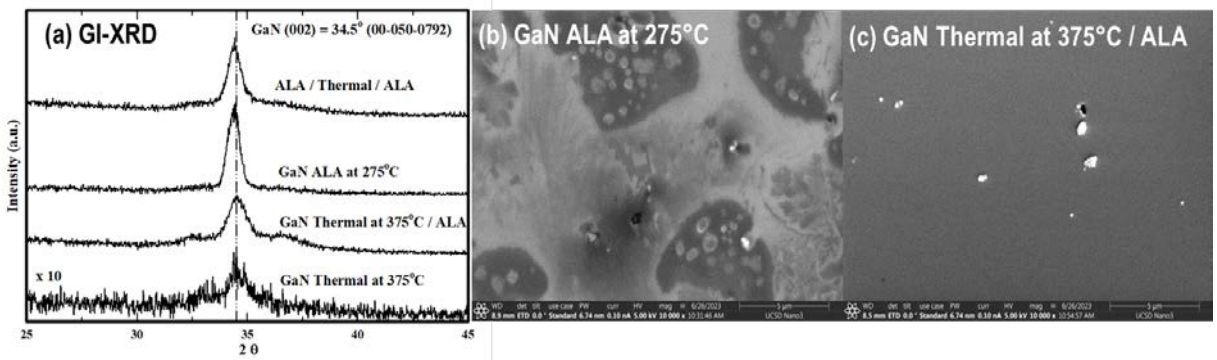

Figure 1. (a) GI-XRD of four GaN ALD layers on Si (111) with different techniques and stacks and (b-c) ex-situ top-view SEM images of KOH wet-etched GaN surface with two different ALD techniques. GaN ALA buffer layer significantly improved the GaN thermal ALD layers and the Ga-polar GaN surface of GaN thermal ALD layers was resistant to KOH wet-etching as compared to the N-polar GaN surface of GaN ALA layers.

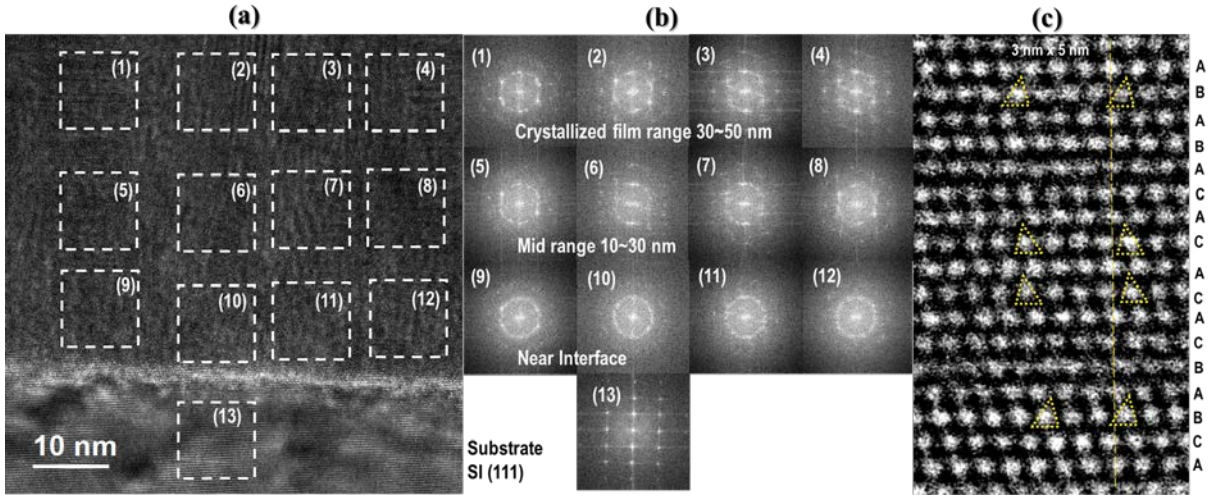

Figure 2. (a) **HR-TEM image, (b) selective area electron digital diffraction patterns, and (c) HAADF-STEM images of GaN ALA on oxide-free Si (111).** Columnar growth of GaN ALD layers in HR-TEM image, improved crystallinity as ALA film growth, and N-polar (upward triangles) GaN observed in HAADF-STEM image.

Presenter: Yun Chen

Lab: Kesong Yang

First principles investigation for helimagnetism in chiral Van der Waals magnets

Abstract: Van der Waals chiral helimagnets have attracted significant research interest recently due to their unique magnetic ordering, strong crystal structural stability and excellent adaptability for the assembly of artificial heterostructures. They are regarded as promising candidates for platforms for next-generation magnetic memories with high storage density, rapid processing speed, and low consumption of energy. However, current research for Dzyaloshinskii-Moriya interaction (DMI) as well as chiral helimagnetism in Van der Waals chiral helimagnets primarily relies on experimental approaches,while theoretical computational research, especially through first principles calculations based on density functional theory (DFT), remains insufficient. In this work, taking Cr1/3NbS2 and Cr1/3TaS2 as examples, utilizing first principles calculations based on DFT, we calculated the value of their magnetic exchange coupling and DMI and investigated their chiral helimagnetism. In addition, we have calculated the Curie temperatures using the Monte Carlo method. This work fills the gap in theoretical first principles calculation research on Van der Waals chiral helimagnet and offers a framework for future computational studies

Presenter's name: Chesson Sipling
Lab: Dr. Massimiliano Di Ventra

Presentation Title: Memory-Induced Long-Range Order in Dynamical Systems

Presentation Abstract: Time non-locality, or memory, is a non-equilibrium property shared by all physical systems. It means that when a system’s state is perturbed, it is still affected by the perturbation at a later time. Here, we show that such a memory effect is sufficient to induce a phase of spatial long-range order (LRO) even if the system’s dynamical variables are coupled locally. This occurs when the memory degrees of freedom have slower dynamics than the system’s degrees of freedom. In addition, such a LRO phase is non-perturbative and attractive to the system, but its existence does not necessarily imply criticality. When the two degrees of freedom have comparable time scales, the length of the effective long-range interaction shortens. We exemplify this behavior with a model of locally coupled spins and a single dynamic memory variable, but our analysis is sufficiently general to suggest that memory could induce a phase of LRO in a much wider variety of physical systems.

Title: Computer-navigated surgery using MRI and Augmented Reality
Presenter: Ananya Rajan, Steven Hui, Songyuan Lu
Advisor: Prof. Frank E.Talke

Abstract: Chronic back pain is a growing global health concern, influenced by an aging population, rising obesity rates, and increasing physical inactivity. With the expected rise in complex back pain cases, there is a pressing need for precise and affordable surgical interventions. Our project focuses on developing an Augmented Reality (AR) surgery navigation system tailored for chronic back pain management. By integrating AR with a 3D personalized spine model which is rebuilt from MRI results, our system offers real-time, three-dimensional guidance during surgeries, enhancing the precision of instrument localization and procedural outcomes. We explore advancements in AR environments, optical tracking, and preclinical modeling, which collectively improve surgical accuracy and patient safety. This approach not only promises to revolutionize back pain surgeries but also aims to provide a cost-effective solution that can be adopted by smaller healthcare facilities, democratizing access to advanced surgical navigation.

Title: Mechanical Behavior of Gyroid Elastomer and Silicone Composite for Simulating Human Soft Tissue

This study aims to analyze the structure and behavior of gyroid geometry for use in composite materials to mimic the mechanical properties of vaginal tissue. A gyroid is a 3D periodic open-cell structure composed of curved surfaces that produce non-linear stress-strain behavior due to the transition from bending-dominated elongation to stretching-dominated elongation with an increase in tension. Nonlinear stress-strain behavior is observed in vaginal tissue, specifically strain-hardening. Strain-hardening is a phenomenon where the tangent modulus of a material increases as it is being stretched, causing the characteristic J-shape stress-strain response of soft tissue. In living vaginal tissue, strain-hardening is attributed to the arrangement and stretching of collagen fibers. To mimic this behavior, a composite composed of a thermoplastic polyurethane (TPU) gyroid scaffold encased in a soft silicone matrix was developed. The principle behind the design of the composite is that during initial stretching, the gyroid will easily elongate as it deforms, but once the gyroid straightens, further elongation is more difficult. In other words, the gyroid in the composite behaves analogous to collagen in tissue.

Finite element analysis (FEA) of various gyroid designs in tension was performed to study the influence of materials properties and design parameters on the desired J-shape stress-strain response. In addition, uniaxial tensile tests were performed to compare numerical and experimental results. We observe that strain softening as well as strain hardening can be achieved by suitable choice of materials and gyroid design parameters, indicating that gyroids are a good choice for simulation of living tissue.

Compact Multispectral Photodetectors based onIntercalated Graphene and Colloidal Quantum Dots

S. Ahn, J.Y. Shang, and O. Vazquez Mena

Center for Memory and Recording Research, Aiiso Yufeng Li Family Department of Chemical and Nano Engineering, Materials Science and Engineering, , University of California San Diego / 9500 Gilman Drive, 92093, La Jolla, USA
ovmena@ucsd.edu

***Abstract*—We construct a hybrid system of intercalated graphene and PbS quantum dots with independent electrical contacts for each graphene layer. This geometry demonstrates a different spectral response for each graphene layer, showing a red shift toward the deeper layers. The intercalated architecture enables probing of the photocurrent depth profile, which can be used for compact multispectral photodetection.**

Keywords—graphene, quantum dots, photodetectors, multispectral, penetration depth, 2D materials

I. Introduction

Compact and broadband photodetectors with spectral analysis capabilities are essential in many material composition applications, such as remote and point-of-care health care, food inspection, and environmental quality monitoring [1]. Current commercial multispectral photodetectors are constructed with filters, lens arrays, beam splitters, and interferometers, which involve large footprints [2]. Nanomaterials, such as 2D materials and quantum dots, are promising candidates for miniaturizing the footprint of multispectral photodetectors [3, 4]. Here, we present a novel architecture of intercalated graphene and PbS quantum dot (QD) hybrid system, with independent electrodes for each intercalated graphene layer. As the depth of the graphene layer increases, the photocurrent wavelength range also red-shifts. Thus, we can extract a photocurrent depth coefficient that can be correlated to each incident wavelength. Our intercalated system of graphene and QDs with independent electrodes can facilitate wavelength identification and spectral analysis, without any dispersive or interferometer components.

II. Optoelectronic Characterizations

Graphene was transferred to the sample substrate using the wet transfer technique. PbS QDs were synthesized using the hot-injection method to obtain a solution of oleic acid functionalized QDs dissolved in toluene. The PbS QD layers were spincoated onto the sample substrate, followed by a ligand exchange step. Photolithography and dry etching were used to define the shape of the graphene and QD layers. After all fabrication steps have been completed, the optoelectronic properties of the intercalated graphene/QD hybrid devices are characterized with a 2400 Keithley sourcemeter and a Xe lamp with a monochromator attached.

Two types of devices were fabricated: Single Bandgap device and Multi-Bandgap device. The Single Bandgap device used only one type of PbS QD, with an exciton peak at 920 nm. It had four graphene layers intercalated. The device stacking scheme is shown in Figure 1a. The Multi-Bandgap device used three types of PbS QDs, with exciton peaks at 850 nm, 1190 nm, and 1350 nm. It had five graphene layers intercalated. The device stacking scheme is shown in Figure 1b.

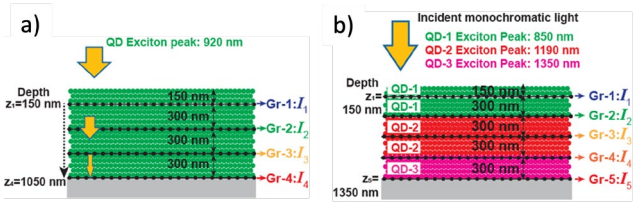

Fig. 1. a) Single Bandgap Device: four graphene layers intercalated with four QD layers, each QD layer has the same type of QD. b) Multi-Bandgap Device: five graphene layers intercalated with five layers of QDs, made of three different sizes.

A. Single Bandgap Device

Figure 2 shows the optoelectronic characterizations of the Single Bandgap device. The photocurrent for each graphene layer as a function of wavelength is shown in Figure 2a. The top graphene layer shows the largest photocurrent, while the bottom layer shows the smallest photocurrent. This is expected, as the top layer experiences the largest photon flux. Figure 2b shows the normalized photocurrent, with respect to the maximum photocurrent of each graphene layer. Over 60% of the photocurrent of Gr-1 ranges between 400-1150 nm, while over 60% of the photocurrent of Gr-4 ranges between 700-1300 nm. The red-shifted range indicates that the longer wavelength photons penetrate deeper into the Gr/QD stack, giving a different photoresponse for each graphene layer. It is possible to identify the wavelength of the incident photon, by examining the relative photoresponses of each graphene layer.

Figure 2c shows the normalized photocurrent as a function of depth for each incident wavelength. From 400 nm to 600 nm, there is an exponential decay in normalized photocurrent; beyond 700 nm, the decay is much slower and the depth profile becomes flat, indicating the same normalized photocurrent for all depths. The depth profiles in Figure 2c were fitted to an exponential function ~exp(-γz), to extract the decay coefficient (see Figure 2d), which we call the "Photocurrent Depth Coefficient (γ)". Shorter wavelengths have higher γ values, and longer wavelengths have lower values, following a similar trend as the absorption coefficient (α). The photocurrent depth coefficients characterize the photodetector wavelength response and can be used to extract spectral information.

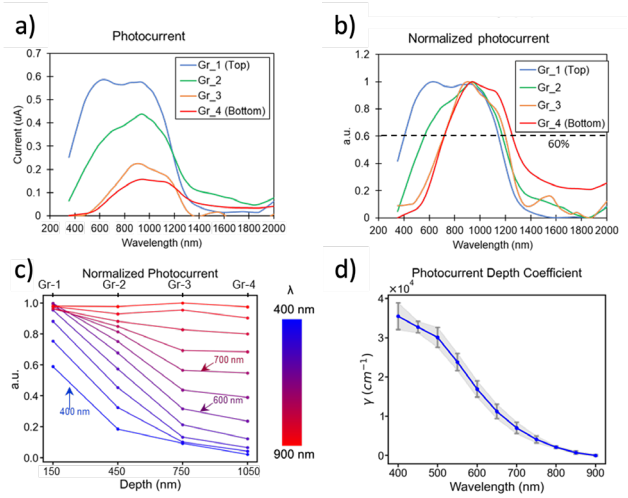

Fig. 2. Optoelectronic characterizations of Single Bandgap Device. a) Photocurrent from each graphene layer (V_{SD} = 0.1 V), showing a different response for each layer. b) Photocurrent normalized to the maximum of each layer, showing a red shift in photocurrent wavelength range toward deeper layers. c) Depth profile of normalized photocurrent for each incident wavelength, derived from b). d) Photocurrent depth coefficient (γ), extracted by fitting an exponential decay to the depth profiles from c).

B. Multi-Bandgap Device

Figure 3 shows the optoelectronic characterizations of the Multi-Bandgap device. The photocurrent for each graphene layer as a function of wavelength is shown in Figure 3a. Gr-3 shows the largest photocurrent, rather than Gr-1. The different behavior in Multi-Bandgap device is due to many factors, such as the differences in absorptivity, photocarrier lifetime, and charge transfer efficiency of QDs of different sizes [5]. Regardless of the absolute value of the photocurrent, the normalized photocurrent values (Figure 3b) show a similar red-shifted trend as the Single Bandgap device. Over 60% of the photocurrent of Gr-1 ranges between 300-950 nm, while over 60% of the photocurrent of Gr-4 ranges between 600-1400 nm. By using three different types of QDs, we have expanded the spectral range of our photodetector, and further differentiated the spectral responses of each graphene layer.

The depth profile of the normalized photocurrent for each incident wavelength is shown in Figure 3c. The extracted photocurrent depth coefficients (γ) are shown in Figure 3d. At the short wavelengths (< 900 nm), the depth profiles follow an exponential decay (positive γ), similar to the Single Bandgap device. From 900 nm to 1400 nm, the depth profile changes to an exponential increase (negative γ), indicating that the normalized photocurrent is higher at deeper levels. Beyond 1400 nm, all three types of QDs are transparent to the incident photons, the absorption and photocurrent approach zero, which leads to a flat depth profile and γ values that also approaches zero. Between 400 nm and 1400 nm, the photocurrent depth coefficients of our Multi-Bandgap device can be correlated to each incident wavelength, enabling wavelength identification and spectral analysis.

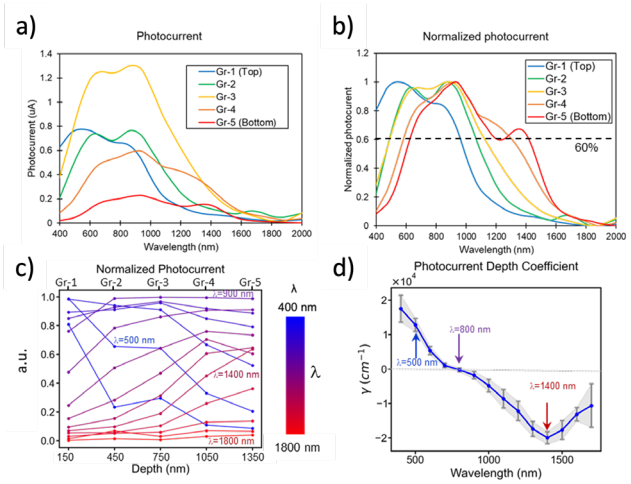

Fig. 3. Optoelectronic characterizations of Multi-Bandgap Device. a) Photocurrent from each graphene layer (V_{SD} = 0.1 V). b) Photocurrent normalized to the maximum of each layer. c) Depth profile of normalized photocurrent for each incident wavelength, derived from b). d) Photocurrent depth coefficient (γ), extracted by fitting an exponential function to the depth profiles from c).

III. Conclusion

We have demonstrated a novel technology of intercalated graphene and QD layers, with independent electrodes for each graphene layer. It is possible to extract photocurrent depth coefficients based on the photoresponses of our devices and correlate them to the wavelength of the incident light source. This technology does not require dispersive or interferometer components, resulting in a compact thin film photodetector with spectral analysis capabilities.

Acknowledgment

This work was supported by the National Science Foundation under Award No. 2046176 (NSF CAREER). This work was performed, in part, at the San Diego Nanotechnology Infrastructure (SDNI) of UCSD, NANO3, a member of the National Nanotechnology Coordinated Infrastructure, which was supported by the National Science Foundation (Grant No. ECCS-1542148). Seungbae Ahn was supported by the Kwanjeong Fellowship from the Kwanjeong Educational Foundation.

References

[1] A. Li *et al.*, "Advances in cost-effective integrated spectrometers," *Light Sci Appl,* vol. 11, no. 1, p. 174, Jun 7 2022, doi: 10.1038/s41377-022-00853-1.

[2] Z. Yang, T. Albrow-Owen, W. Cai, and T. Hasan, "Miniaturization of optical spectrometers," *Science,* vol. 371, no. 6528, Jan 29 2021, doi: 10.1126/science.abe0722.

[3] S. Yuan, D. Naveh, K. Watanabe, T. Taniguchi, and F. Xia, "A wavelength-scale black phosphorus spectrometer," *Nature Photonics,* vol. 15, no. 8, pp. 601-607, 2021, doi: 10.1038/s41566-021-00787-x.

[4] X. Tang, M. M. Ackerman, M. Chen, and P. Guyot-Sionnest, "Dual-band infrared imaging using stacked colloidal quantum dot photodiodes," *Nature Photonics,* vol. 13, no. 4, pp. 277-282, 2019, doi: 10.1038/s41566-019-0362-1.

[5] S. Ahn and O. Vazquez-Mena, "Measuring the carrier diffusion length in quantum dot films using graphene as photocarrier density probe," *J Chem Phys,* vol. 156, no. 2, p. 024702, Jan 14 2022, doi: 10.1063/5.0071119.

Title: Searching for next-generation battery materials

Speaker: Ping Liu

Rechargeable batteries have powered the transition to electrified transportation and promise to transform the electric grid. At the Sustainable Power and Energy Center (SPEC) at UC San Diego, we work with our industrial and government partners to develop batteries that can charge faster, cycle longer, use more abundant materials, work under extreme temperatures, and can be recycled more easily. In this talk we will offer a few examples to illustrate our approaches to the discovery of new materials and their translation into technologies. One specific example is a solid-state lithium-sulfur battery that employs a sulfur-iodine (S-I) cathode material. Sulfur, as an electrode material, has long suffered from very a low electronic conductivity and large volume changes during operation. These challenges have led to poor material utilization and cycling stability. The S-I material features a semi-conductor level electronic conductivity and a melting point of 65^{o}C. These features have enabled high utilization as well as the ability to heal the degraded battery structure by remelting the cathode. We conclude by offering perspectives for future directions of battery development.

Outer Code Designs for Augmented and Local-Global Polar Code Architectures

Presenter: ***Ziyuan Zhu***, PhD student, ECE

Researcher: ***Ziyuan Zhu***, PhD Student, ECE

Advisor: ***Paul H. Siegel,*** Professor, ECE/CMRR

We introduce two novel methods to design outer polar codes for two previously proposed concatenated polar code architectures: augmented polar codes [1] and local-global polar codes [2]. These methods include a stopping set (SS) construction and a nonstationary density evolution (NDE) construction. The stopping set design is based on previous work on conventional polar codes [3]. Simulation results demonstrate the advantage of these methods over previously proposed constructions based on density evolution (DE) and LLR evolution.

[1] A. Elkelesh, M. Ebada, S. Cammerer and S. t. Brink, “Flexible Length Polar Codes through Graph Based Augmentation,” SCC 2017; 11th International ITG Conference on Systems, Communications and Coding, 2017, pp. 1-6.

[2] Z. Zhu, W. Wu and P. H. Siegel, “Polar Codes with Local-Global Decoding,” 2022 56th Asilomar Conference on Signals, Systems, and Computers, Pacific Grove, CA, USA, 2022, pp. 392-396, doi: 10.1109/IEEECONF56349.2022.10051996.

[3] A. Eslami and H. Pishro-Nik, “On Finite-Length Performance of Polar Codes: Stopping Sets, Error Floor, and Concatenated Design,” IEEE Transactions on Communications, vol. 61, no. 3, pp. 919-929, March 2013.

The Labeled Coupon Collector Problem

Presenter: ***Andrew Tan,*** PhD Student, ECE

Researcher: ***Andrew Tan,*** PhD Student, ECE

Advisor: ***Paul Siegel***, Professor, ECE/CMRR

Abstract:

A combinatorial problem with applications to DNA watermarking can be stated concisely as follows:

Suppose n objects are each associated with a distinct label, where the set of all labels is known a priori. To help identify the labels of each object, you can draw k objects uniformly at random and obtain their labels in a random order, where k is between 1 and $n-1$. How many draws are you expected to make in order to identify the labels of all n objects? What is the minimum number of draws required?

This problem suggests a similarity to the well-known Coupon Collector Problem (CCP) [1] in probability theory. In fact, it becomes a variation of this problem when $k = 1$ or $k = n - 1$.

For these reasons, we call the above problem the Labeled Coupon Collector Problem (LCCP).

In this talk, we will introduce the problem rigorously and provide our current understanding towards solving it, with special attention given to the case where $k = 2$. We will introduce a simple algorithm that can simulate the problem and give the empirical distribution and statistics for the number of draws for any value of n and k. For the special case of $k = 2$, we find a closed-form expression for the minimum number of draws as well as introduce a promising method based on the absorbing states of Markov chains [2],[3] to help compute an exact expression for the expected number of draws, which we have validated for $n = 3, 4, 5, 6$.

[1] Wikipedia contributors. (2024, February 9). Coupon collector's problem. In Wikipedia, The Free Encyclopedia. Retrieved 18:18, May 30, 2024, from https://en.wikipedia.org/w/index.php?title=Coupon_collector%27s_problem&oldid=1205223195

[2] Wikipedia contributors. (2024, May 25). Absorbing Markov chain. In Wikipedia, The Free Encyclopedia. Retrieved 18:29, May 30, 2024, from https://en.wikipedia.org/w/index.php?title=Absorbing_Markov_chain&oldid=1225622508

[3] J. R. Norris, *Markov Chains.* New York: Cambridge University Press, 1997, ch. 1, p. 17.

Functional Error Correction for Vision-Language Models

Presenter: ***Wenyu Peng***, PhD Student, ECE

Researcher: ***Wenyu Peng***, PhD Student, ECE

Advisor: ***Paul H. Siegel,*** Professor, ECE/CMRR

Collaborator: Simeng Zheng, PhD Student, ECE

When implementing a neural network (NeuralNet) in hardware, it is crucial to store its weights in memory devices. However, the accumulation of noise in the stored weights can lead to a degradation in the NeuralNet's performance, such as retention errors [1]. Unlike traditional error correction techniques employed in data storage, the goal here is to enhance the NeuralNet's performance after error correction, rather than solely minimizing the Uncorrectable Bit Error Rate in the protected bits. A significant challenge arises due to the deep nature of NeuralNets, which often contain millions to hundreds of millions of weights, resulting in a substantial redundancy overhead for error correction codes (ECCs). Additionally, the relationship between the weights and the NeuralNet's performance can be highly intricate.

A selection protection scheme has demonstrated a better performance-redundancy trade-off by selecting the most important bits for protection [2]. This scheme employs Reinforcement Learning to identify the most crucial bits across different layers. However, previous work has only focused on VGG-16 [3] and ResNet-18 [4] models for image classification tasks, which have relatively simple network structures.

In this work, we extend the approach in [1] to the CLIP (Contrastive Language-Image Pre-Training) model, a large Vision-Language Model trained on image-text pairs [5]. Furthermore, we consider the task of “zero-shot” prediction, where CLIP automatically labels a given image with text. Experimental results show that the selection protection scheme can also perform well with a complex model and in the context of a “zero-shot” prediction task.

[1] P. Upadhyaya, X. Yu, J. Mink, et al., “Error correction for hardware-implemented deep neural networks,” Proc. Non-Volatile Memories Workshop. 2019: 1-2.

[2] K. Huang, P. H. Siegel, A. Jiang, “Functional error correction for robust neural networks,” IEEE Journal on Selected Areas in Information Theory, 2020, 1(1): 267-276.

[3] S. Karen, “Very deep convolutional networks for large-scale image recognition,” arXiv preprint arXiv: 1409.1556, 2014.

[4] K. He, X. Zhang, S. Ren, et al., “Deep residual learning for image recognition,” Proceedings of the IEEE Conference on Computer Vision and Pattern Recognition. 2016: 770-778.

[5] A. Radford, J W. Kim, C. Hallacy, et al., “Learning transferable visual models from natural language supervision,” International Conference on Machine Learning. PMLR, 2021: 8748-8763.

Presenter: Tianxing Wang
Lab: Prof. Ivan Schuller

Presentation Title: Controlling magnetic properties with phase transition metal oxides

Presentation Abstract: Interfacial effects between antiferromagnetic (AFM) and ferromagnetic (FM) materials have long been a center of magnetism studies. The most prominent of which is exchange bias, an interfacial effect indispensable for modern day's hard disk drives. Aside from the exchange bias, controlling the coercivity is another significant topic in magnetic recordings. In this talk, we present the use of metal oxide thin films that exhibit phase transitions to control the magnetic properties of FM layer in AFM/FM heterostructures, specifically with vanadium sesquioxide (V_2O_3) and hematite (α-Fe_2O_3) when coupled with a soft ferromagnet permalloy (NiFe). We report significant exchange bias at the onset of the metal-to-insulator transition (MIT) of vanadium sesquioxide (V_2O_3). The strongly coupled electronic, magnetic and structural properties in V_2O_3 allows the magnetic phase transition to be triggered not only by temperature but also by applying electric field, strain and local heat. These additional switching methods of the V_2O_3's magnetic phase have the potential for multifunctional applications. Moreover, we present the coercivity enhancement across the Morin transition in hematite (α-Fe_2O_3)/permalloy bilayers, where the temperature-triggered spin reorientation in hematite causes sizable increase in the coercive field of permalloy. Through these results, we show the possible new functionalities that can be enabled by phase transitions in metal oxides when used in AFM/FM heterostructures and be used as an additional nob for post-growth control of magnetic properties.

Presenter: Nareg Ghazikhanian
Lab Group: Dr. Ivan Schuller

Filament localization and tuning of resistive switching phenomena via selective ion irradiation

Abstract:

Various materials exhibit resistive switching, a useful feature which lends well to the development of novel bioinspired electronic devices, notably artificial neurons and synapses for neuromorphic computing. In a number of material systems, this effect occurs through the percolation of conducting filaments across an otherwise insulating matrix. Often, the location and switching parameters of the resistive switching are impacted by inherent material defects, which poses a serious challenge for scalability of neuromorphic circuits. By selectively engineering defects using a focused ion beam, we report a novel method of locally tuning a material's electronic properties (i.e. conductivity and metal-insulator transition temperature) and by extension, controlling the location and geometry of the conducting filament. In addition to confining the conducting filament to the irradiated region, we observe a greater than 3 orders of magnitude reduction in resistive switching power. Furthermore, we observe emergent stochastic phenomena. Our work demonstrates that local ion irradiation is an efficient tool for fine-tuning material properties related to resistive switching. This offers promising avenues for new energy-efficient biomimetic circuitry.

This work was supported by the Air Force Office of Scientific Research under Award No. FA9550-22-1-0135. Device fabrication and irradiation were carried out at the NANO3 cleanroom facility at UC San Diego.

Effects on the electronic and magnetic transitions by light in $CdS/La_{0.7}Sr_{0.3}MnO_3$ heterostructures

Presenter: **Dr. Henry Navarro**

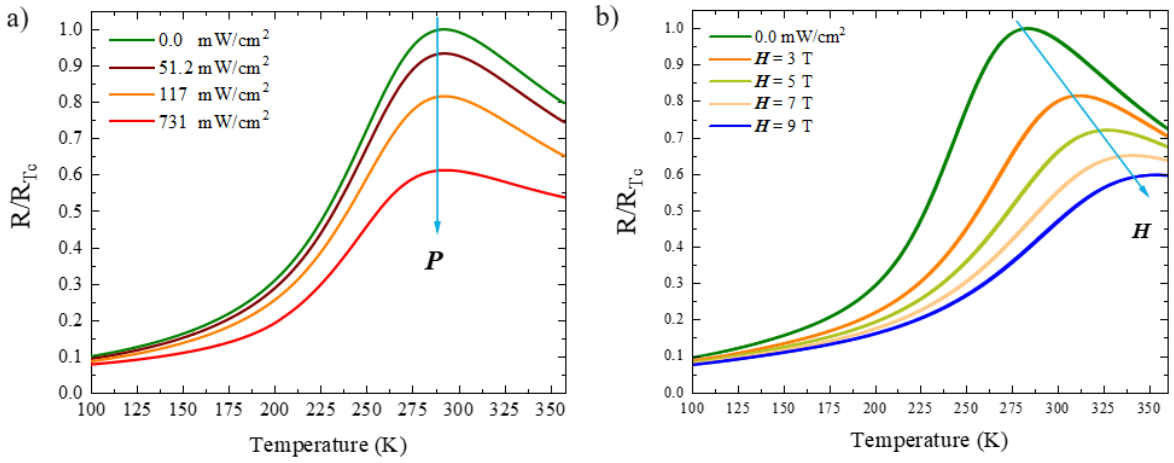

Figure: Light-induced modification of the metal-to-insulator transition in CdS/LSMO heterostructures. Resistance versus temperature $R(T)$ measurements for hybrid CdS/LSMO heterostructures, for (a) varying light power density and (b) varying magnetic field. The dashed lines in (b) shows the effect of 42-mW/cm^2 light for selected magnetic fields (0, 3, and 9 T). The solid green curves correspond to resistance versus temperature without light in all panels.

The strongly correlated material $La_{0.7}Sr_{0.3}MnO_3$ (LSMO) exhibits metal-to-insulator and magnetic transition near room temperature. Although the physical properties of LSMO can be manipulated by strain, chemical doping, temperature, or magnetic field, they often require large external stimuli. To include additional flexibility and tunability, we developed a hybrid optoelectronic heterostructure that uses photocarrier injection from cadmium sulfide (CdS) to an LSMO layer to change its electrical conductivity. LSMO exhibits no significant optical response; however, the CdS/LSMO heterostructures show an enhanced conductivity, with a resistance drop of about 37%, at the transition temperature under light stimuli. This enhanced conductivity in response to light is comparable to the effect of a 9 T magnetic field in pure LSMO. Surprisingly, the optical and magnetic responses of CdS/LSMO heterostructures are decoupled and exhibit different effects when both stimuli are applied [1]. This unexpected behavior shows that heterostructuring strongly correlated oxides may require a new understanding of the coupling of physical properties across the transitions and provide the means to implement new functionalities.

The synthesis of the heterostructures and measurement of transport, magnetic, and optical properties were supported by the U.S. Department of Energy's Office of Basic Energy Science, under Grant DE-FG02-87ER45332, the synthesis of LSMO by the Spanish MCI through Grants No. MAT 2017-87134-C02 and No. PCI 2020-112093, and theory by the French ANR "MoMA" project ANR-19-CE30-0020, Chilean FONDECYT 1211902, and Basal AFB220001.

[1] H. Navarro et al. "Light-Induced Decoupling of Electronic and Magnetic Properties in Manganites". *Physical Review Applied* 19 (2023) 044077.

Abstract for CMRR review

Student: Jiawei Duan

Professor: Vitaliy Lomakin

Soft magnetic materials play a critical role in high-frequency applications, such as transformers, inductors, and electromagnetic shielding. Their low coercivity and high permeability make them ideal for efficient magnetic flux control. I want to present some progress on the modeling of soft magnetic materials, particularly by incorporating the effects of eddy currents. Our approach enables the modeling of grain sizes up to micrometers, allowing for detailed analysis of various magnetic behaviors.

We examine the BH loop, hysteresis loss, and dynamic responses of these materials under different conditions. Specifically, we investigate the losses under a DC magnetic field, as well as in demagnetized and remanent states. Additionally, our models consider the effects of different interface exchange couplings on the material's behavior.

Also, our methods leverage advanced finite element modeling techniques, integrating electromagnetic solvers with micromagnetic solvers to accurately simulate the combined magnetization and eddy current dynamics. This integration allows for a comprehensive understanding of the material's performance in real-world applications, providing insights into optimizing material design and improving device efficiency.

The outcomes of this research enhance our ability to predict the behavior of soft magnetic materials, paving the way for more efficient and effective magnetic devices.

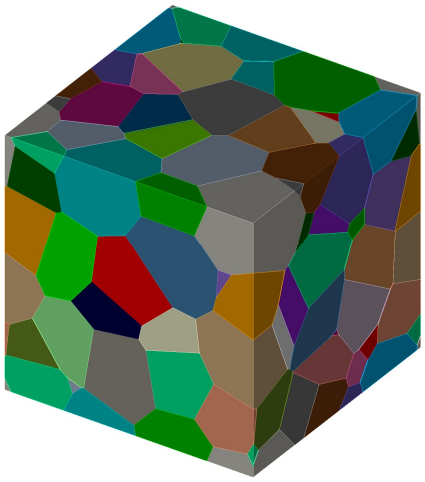

Fig. 1. Modeling of a block of soft material has 60 grains of size 2 um.

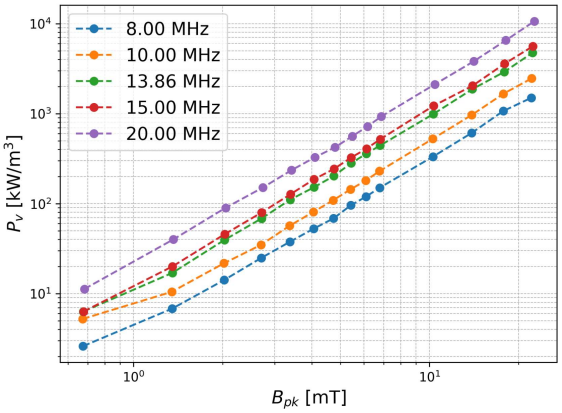

Fig.2 Core loss at different frequencies and applied field